Presented at 69th International Astronautical Congress (IAC), Bremen, Germany, 1-5 October 2018.

https://iafastro.directory/iac/paper/id/43317/summary/

IAC-18-C1.9.9

# Low-energy trajectory design and autonomous navigation to flyby near-Earth asteroids using CubeSats

**Pablo Machuca[a,*], Joan Pau Sánchez[b], Josep J. Masdemont[c], Gerard Gómez[d]**

[a] *Space Research Group, Cranfield University, College Road, Cranfield, Bedfordshire, United Kingdom MK43 0AL,* p.machuca@cranfield.ac.uk
[b] *Space Research Group, Cranfield University, College Road, Cranfield, Bedfordshire, United Kingdom MK43 0AL,* jp.sanchez@cranfield.ac.uk
[c] *IEEC & Departament de Matemàtiques, Universitat Politècnica de Catalunya, Diagonal 647, Barcelona, Catalunya, Spain 08028,* josep.masdemont@upc.edu
[d] *IEEC & Departament de Matemàtiques i Informàtica, Universitat de Barcelona, Gran Via 585, Barcelona, Catalunya, Spain 08007,* gerard@maia.ub.es

* Corresponding Author

**Abstract**

In response to the current interest in CubeSats and potential applications for planetary exploration, this work studies the feasibility of using autonomous CubeSats to flyby near-Earth asteroids. Considering the limited performance of current propulsion systems for CubeSats, low-energy (impulsive and low-thrust) trajectories are designed to encounter near-Earth asteroids in the medium-fidelity Circular Restricted Three-Body Problem, and their existence in a high-fidelity ephemeris model is also verified. The use of large ground antennas for deep-space communications might represent a major portion of CubeSat mission budgets, and thus the feasibility of performing optical navigation to autonomously estimate and correct the trajectory of the CubeSat is also evaluated through Monte Carlo simulations. Preliminary results show that approximately 4 asteroids per year could be reached by a 3U CubeSat if deployed around the first or second Sun-Earth Lagrange points. According to the limited performance of current CubeSat components, flyby altitudes of the order of 100–500 kilometers are determined possible using only observations of the Sun and of the target asteroid for autonomous navigation.
**Keywords:** Interplanetary CubeSats; near-Earth asteroids; trajectory design; autonomous navigation

**Nomenclature**

| | |
|---|---|
| $\Delta V$ | Velocity increment |
| $x^A$, $y^A$, $z^A$ | Cartesian position coordinates expressed in reference frame $A$ |
| $v_x^A$, $v_y^A$, $v_z^A$ | Cartesian velocity coordinates expressed in reference frame $A$ |
| $\bar{x}^A$ | Cartesian state vector (position and velocity coordinates) expressed in reference frame $A$ |
| $\bar{x}^A(t)_i$ | $i$-th component of vector $\bar{x}$ at time $t$ expressed in reference frame $A$ |
| $\bar{r}^A$, $\bar{v}^A$, $\bar{a}^A$ | Cartesian position, velocity and acceleration vectors expressed in reference frame $A$ |
| $\bar{r}_i$, $\bar{v}_i$, $\bar{a}_i$ | Position, velocity and acceleration vectors of body $i$ |
| $\bar{r}_{i\to j}$, $\bar{v}_{i\to j}$, $\bar{a}_{i\to j}$ | Position, velocity and acceleration vectors of body $j$ with respect to body $i$ |
| ${}^A\hat{x}^B$, ${}^A\hat{y}^B$, ${}^A\hat{z}^B$ | Cartesian unit vectors of reference frame $B$ expressed in reference frame $A$ |
| $\mu$ | CR3BP mass parameter |
| $d, r$ | CR3BP relative distance to first and second primaries |
| $m_i$ | Mass of body $i$ |
| $m^*, l^*, t^*$ | Characteristic CR3BP mass, length and time |
| $\tilde{t}$ | CR3BP non-dimensional time |
| $G$ | Universal gravitational constant |
| $\Phi(t_2, t_1)$ | State-transition matrix from time $t_1$ to time $t_2$ |
| $\Phi(t_2, t_1)_{i,j}$ | $i$-th row and $j$-th column component of the state-transition matrix from time $t_1$ to time $t_2$ |
| $A(t)$ | Jacobian matrix of non-linear equations of motion |
| $I_{m\times m}$ | $m \times m$ identity matrix |
| ${}^AC^B$ | Rotation matrix from reference frame $B$ to reference frame $A$ |
| $\bar{b}$ | Position vector of common barycenter of Sun and Earth-Moon system |
| $n$ | Number of planetary bodies considered in the ephemeris model |
| $\delta v_j^+$, $\delta v_j^-$ | Small variation along positive and negative $j$-th component of the velocity |

| | |
|---|---|
| $\varepsilon, \theta$ | Elevation and azimuth angles of velocity vector in CR3BP |
| $m$ | Mass of the spacecraft |
| $\bar{T}^A$ | Thrust vector expressed in reference frame $A$ |
| $T_x^A$, $T_y^A$, $T_z^A$ | Thrust vector cartesian components expressed in reference frame $A$ |
| $I_{sp}$ | Non-impulsive thruster specific impulse |
| $g_0$ | Non-dimensional gravitational acceleration at sea level |
| σ | Standard deviation |

**Acronyms/Abbreviations**

| | |
|---|---|
| L1, L2 | First and second Lagrange points |
| CR3BP | Circular Restricted Three-Body Problem |
| EMB | Earth-Moon barycenter |
| U | CubeSat basic unit (10 cm x 10 cm x 10 cm) |
| Navcam | Navigation camera |
| PUC | Propulsion Unit for CubeSats |
| EoM | Equations of motion |
| AU | Astronomical unit |
| STM | State-transition matrix |
| NLP | Non-linear programming |
| ADCS | Attitude determination and control system |
| BCT | Blue Canyon Technologies |
| TCM | Trajectory correction maneuver |

## 1. Introduction

CubeSat technology has rapidly evolved over the past decade and numerous missions have been launched to low-Earth orbit for technology demonstration, scientific or commercial purposes [1–3]. The first interplanetary CubeSat mission, MarCO, was launched in 2018 to flyby Mars and provide communications support to NASA's InSight mission [4,5]. CubeSats have gathered great interest from the scientific community and are now also viewed as a potential low-cost solution for the exploration of the Solar System, with missions planned to observe and land on the Moon or to flyby a near-Earth asteroid (NEA Scout mission) [6–8].

In the context of increasing interest in CubeSat technology and potential applications for planetary exploration, this works studies the feasibility of using autonomous CubeSats to flyby near-Earth asteroids.

The first (L1) and second (L2) Sun-Earth Lagrange points are common destinations for scientific missions to study the Sun and outer space [9–11], and future missions to these points could provide a piggyback opportunity to deploy a CubeSat and flyby an asteroid passing close to the Earth [12–14]. Low-ΔV impulsive and low-thrust trajectories are designed in this work to encounter near-Earth asteroids from halo orbits around L1 and L2, considering the stringent propulsive capabilities of current CubeSat technology (e.g., low total ΔV, low thrust magnitude, etc.) [15].

Asteroid flyby trajectories are designed first in the medium-fidelity Circular Restricted Three-Body Problem (CR3BP) [16–18], considering solely the gravitational influences of the Sun and the Earth-Moon barycenter (EMB), and then results are verified in a high-fidelity ephemeris model considering the actual positions and gravitational attractions of the major influencing bodies in the Solar System.

The feasibility of performing autonomous optical navigation to estimate and correct the trajectory of the CubeSat prior to the flyby is also evaluated. A simple autonomous navigation campaign is considered using only observations of the Sun during cruise, and observations of the target asteroid once it becomes visible by the on-board navigation camera (navcam). Monte Carlo simulations are performed to understand the effect of the limited performance of current CubeSat sensors and actuators on the resulting flyby accuracies (e.g., inaccuracies in the propulsive maneuvers, uncertainties in the departure position and velocity, navcam performance, etc.).

Through a trajectory design and autonomous navigation analysis, this work effectively evaluates the readiness level of current CubeSat technology to provide a low-cost solution to flyby near-Earth asteroids and perform significant science.

The design of low-ΔV impulsive and low-thrust trajectories in the CR3BP and ephemeris models is described in Section 2, the sensitivity analysis and autonomous navigation strategy are described in Section 3, results are shown and discussed in Section 4.

## 2. Design of low-energy asteroid flyby trajectories

In order to reach near-Earth asteroids, and considering the limited propulsive capabilities of CubeSats, a piggyback opportunity to periodic orbits around the first or second Sun-Earth Lagrange points is leveraged. These periodic orbits are commonly used by large scientific missions, and a few missions are also planned for the mid-2020s (James Webb Space Telescope [12], ARIEL [13], PLATO [14], etc.).

In specific, departure halo orbits of equivalent size to those used by the LISA Pathfinder mission around L1 and by the James Webb Space Telescope around L2 (~500,000 km x 1,500,000 km x 800,000 km) are employed in this work [11,12].

Trajectories to flyby near-Earth asteroids departing from halo orbits around L1 and L2 are designed for two thrusting cases: (1) the on-board thruster can generate impulsive or quasi-impulsive changes in velocity (Sections 2.3 and 2.4), and (2) the on-board thruster is a low-thrust propulsion system (Section 2.5). The total available ΔV considered for the impulsive and low-thrust trajectories is 80 m/s, which could be generated,

respectively, by VACCO's 0.5U, 5-mN warm-gas Propulsion Unit for CubeSats (PUC) [19], or Busek's 0.4U, 100μN electrospray BET-100 propulsion system [20] (assuming a 4-kg, 3U CubeSat).

It is worth mentioning that current propulsion systems for CubeSats have also strong limitations in terms of their nominal thrust magnitudes (usually of the order of a few millinewtons) and might require low thrusting times to generate their total ΔV (e.g., VACCO's PUC requires about 35 hours to produce its 80-m/s change in velocity, in thrusting cycles of 20 minutes on, and 20 minutes off for cooling down). As such, impulsive maneuver trajectories (like the low-ΔV impulsive trajectories discussed in Section 2.3) can serve as a first approximation but might require additional refinement and more realistic thruster models depending on the desired level of fidelity (further addressed in Section 2.4).

Lastly, the timespan for the mission is specifically constrained to 150 days in an effort to propose short-duration (and effectively lower-cost) asteroid flyby solutions for future CubeSat missions. And the time window considered for the mission spans between years 2019 and 2025, although the methodology described in the following sections can be directly applied to other time windows.

### *2.1. Circular Restricted Three-Body Problem (CR3BP)*

The CR3BP has been and is extensively used for the preliminary design of trajectories in applications in which the predominant gravitational influences on the dynamics of a body of interest (e.g., spacecraft) can be described by that of two main planetary bodies orbiting each other (e.g., trajectories in the Earth-Moon system, trajectories primarily influenced by the Sun and Jupiter, trajectories primarily influenced by the Sun and the Earth, etc.) [21,22].

In this work, the interest is focused on asteroid flyby trajectories departing from periodic orbits around the Sun-EMB Lagrange points, which are primarily influenced by the gravitational attractions of the Sun and the EMB. The CR3BP model is thus used for a preliminary analysis of asteroid flyby trajectories in the neighborhood of the EMB, and conclusions drawn from this analysis are then verified in the higher-fidelity ephemeris model.

The dynamics of a third, massless body in the CR3BP (e.g., spacecraft) are described as a function of the relative positions with respect to the two primaries (e.g., Sun and EMB). The non-dimensionalized equations of motion (EoM) of the CR3BP can be found in numerous references in literature, and are summarized in Eq. (1) for completeness (expressed in the Sun-EMB synodic reference frame and centered at the Sun-EMB barycenter) [16].

$$\begin{aligned}
\frac{dv_x^S}{d\tilde{t}} = \frac{d^2x^S}{d\tilde{t}^2} &= -(1-\mu)\frac{(x^S+\mu)}{d^3} \\
&\quad -\mu\frac{(x^S-1+\mu)}{r^3} + x^S \\
&\quad + 2v_y^S \\
\frac{dv_y^S}{d\tilde{t}} = \frac{d^2y^S}{d\tilde{t}^2} &= -(1-\mu)\frac{y^S}{d^3} - \mu\frac{y^S}{r^3} \\
&\quad + y^S - 2v_x^S \\
\frac{dv_z^S}{d\tilde{t}} = \frac{d^2z^S}{d\tilde{t}^2} &= -(1-\mu)\frac{z^S}{d^3} - \mu\frac{z^S}{r^3}
\end{aligned} \tag{1}$$

where $\bar{x}^S = \left(x^S, y^S, z^S, v_x^S, v_y^S, v_z^S\right)^T$ defines the non-dimensional state vector (cartesian position and velocity coordinates in the non-inertial synodic reference frame), and the mass parameter is defined as $\mu = \frac{m_{EMB}}{m^*}$, with $m^* = m_{Sun} + m_{EMB}$ (characteristic mass). Finally, the characteristic quantities used to non-dimensionalize the EoM are $l^*$ (characteristic length, defined as the nominal distance between the primaries), and $t^* = \sqrt{l^{*3}/(G \cdot m^*)}$ (characteristic time).

The first step in the trajectory design process is to obtain periodic orbits around the Sun-Earth Lagrange points along which the CubeSat is assumed to be deployed, and from which asteroid flyby trajectories are to be designed. Analysis through halo orbits, in particular, offer an insightful view for mission planning and are considered as the departure periodic orbits around L1 and L2 in this work [23–25].

Halo orbits can be analytically approximated to high orders [26,27], and such approximations can then be used as the first guess in the search of an initial state vector that will yield a periodic motion around the Lagrange points (i.e., single-shooting method). This search is generally performed through an iterative Newton differential corrector in terms of the state-transition matrix (STM) [28].

The state-transition matrix is a relevant entity for the generation of periodic orbits around L1 and L2, and for the design of asteroid flyby trajectories. The STM can be numerically propagated at time $t$ as a function of its current value, $\Phi(t, t_0)$ (STM from the initial time, $t_0$, to time $t$), through Eq. (2):

$$\dot{\Phi}(t, t_0) = A(t)\Phi(t, t_0) \tag{2}$$

where $A(t)$ is the Jacobian matrix (partial derivatives of the EoM with respect to the state vector $\bar{x}^S$) of the non-linear system described by Eq. (1), evaluated at the current time $t$. The initial condition for the propagation of the STM is $\Phi(t_0, t_0) = I_{6\times6}$ (6x6 identity matrix).

The STM linearly relates the variation in the initial state, $\delta\bar{x}(t_0)$, to the resulting variation in the final state, $\delta\bar{x}(t_f)$, as described in Eq. (3).

$$\delta\bar{x}(t_f) = \Phi(t_f, t_0)\delta\bar{x}(t_0) \qquad (3)$$

From Eq. (3) one can obtain the approximated change in the initial state required to achieve a desired change in the final state, in such a way that, for instance, the motion described after one revolution is periodic, and also to compute the required change in velocity (i.e., ΔV) to encounter the trajectory of a target asteroid (although this is discussed more in detail in Section 2.3). This operation should be performed iteratively until the updated initial state results in a final state that satisfies the desired conditions within a certain threshold.

*2.2. Ephemeris model*

The first preliminary step to designing trajectories in an ephemeris model is retrieving positions, velocities and accelerations of the planetary bodies of interest as a function of time (i.e., Sun, EMB, Mars, Jupiter and Saturn). Such operation is thoroughly described in literature and primarily consists in the following [29]: (1) read ephemeris file (e.g., DE403, DE430, etc.) containing Chebyshev coefficients for the interpolation of planetary bodies' positions, and (2) compute planetary bodies' positions by evaluating Chebyshev polynomials with the corresponding set of Chebyshev coefficients (and evaluate the first and second time derivatives of those polynomials to compute velocities and accelerations).

The second preliminary step is performing a reference frame transformation between the non-dimensional, synodic and Sun-EMB barycenter-centered representation used in the CR3BP, and the dimensional, inertial and Solar System barycenter-centered representation used by the ephemeris files (generally expressed in the J2000 reference frame). The transformation of a position vector from the CR3BP synodic reference frame to an inertial reference frame can be mathematically expressed as in Eq. (4) [27]:

$$\bar{r}^I = l^* \cdot {}^I C^S \cdot \bar{r}^S + \bar{b}^I \qquad (4)$$

where $\bar{r}^I = (x^I, y^I, z^I)^T$ and $\bar{r}^S = (x^S, y^S, z^S)^T$ represent the cartesian position state vectors expressed in the (dimensionalized) inertial and (non-dimensionalized) synodic reference frames, respectively, and ${}^I C^S$ is the rotation matrix from the synodic reference frame to the inertial reference frame.

All transformation elements in Eq. (4) are time dependent and functions of the position and velocity state vectors of the Sun and the EMB expressed in the inertial reference frame. Specifically, $l^*(t) = |\bar{r}^I_{Sun\to EMB}| = |\bar{r}^I_{EMB} - \bar{r}^I_{Sun}|$ is the norm of the vector from the Sun to the EMB, $\bar{b}^I(t) = \frac{m_{EMB}\cdot\bar{r}^I_{EMB} + m_{Sun}\cdot\bar{r}^I_{Sun}}{m^*}$ is the position of the common Sun-EMB barycenter, and ${}^I C^S$ is defined as in Eq. (5).

$${}^I C^S(t) = [{}^I\hat{x}^S, \quad {}^I\hat{y}^S, \quad {}^I\hat{z}^S] = \left[\frac{\bar{r}^I_{Sun\to EMB}}{|\bar{r}^I_{Sun\to EMB}|}, \quad {}^I\hat{z}^S \times {}^I\hat{x}^S, \quad \frac{\bar{r}^I_{Sun\to EMB} \times \bar{v}^I_{Sun\to EMB}}{|\bar{r}^I_{Sun\to EMB} \times \bar{v}^I_{Sun\to EMB}|}\right] \qquad (5)$$

where $({}^I\hat{x}^S, {}^I\hat{y}^S, {}^I\hat{z}^S)$ are the instantaneous unit vectors of the synodic reference frame expressed in the inertial reference frame.

In order to transform velocity vectors from the synodic to the inertial reference frame, it is necessary to take the derivative of Eq. (4) with respect to time:

$$\bar{v}^I = \frac{dl^*}{dt} \cdot {}^I C^S \cdot \bar{r}^S + l^* \cdot \frac{d\,{}^I C^S}{dt} \cdot \bar{r}^S + \frac{l^*}{t^*} \cdot {}^I C^S \cdot \bar{v}^S + \frac{d\bar{b}^I}{dt} \qquad (6)$$

where $t^*$ is defined as the inverse of the average mean motion of the Sun-EMB system, and is used to dimensionalize the time derivative of the position vector $\bar{r}^S$ (i.e., $\bar{v}^S = d\bar{r}^S/d\tilde{t}$).

The EoM that describe the dynamics of a massless spacecraft under the gravitational influence of $n$ planetary bodies (i.e., $n$-body problem) are summarized in Eq. (7), and are used for the propagation of trajectories in an ephemeris model [30]:

$$\begin{aligned} \frac{dv^I_x}{dt} &= \frac{d^2x^I}{dt^2} = -G\sum_{i=1}^{n} m_i \frac{(x^I - x^I_i)}{|\bar{r}^I - \bar{r}^I_i|^3} \\ \frac{dv^I_y}{dt} &= \frac{d^2y^I}{dt^2} = -G\sum_{i=1}^{n} m_i \frac{(y^I - y^I_i)}{|\bar{r}^I - \bar{r}^I_i|^3} \\ \frac{dv^I_z}{dt} &= \frac{d^2z^I}{dt^2} = -G\sum_{i=1}^{n} m_i \frac{(z^I - z^I_i)}{|\bar{r}^I - \bar{r}^I_i|^3} \end{aligned} \qquad (7)$$

where $\bar{x}^I = \left(x^I, y^I, z^I, v^I_x, v^I_y, v^I_z\right)^T$ is the dimensional state vector (cartesian position and velocity coordinates in inertial reference frame), and $\bar{r}^I_i = (x^I_i, y^I_i, z^I_i)^T$ is the position vector of each planetary body $i$ considered.

The STM in the ephemeris model can be propagated according to Eq. (2) as discussed in Section 2.1, where the Jacobian matrix $A(t)$ is now defined as the partial derivatives of the system described in Eq. (7) with respect to the state vector $\bar{x}^I$.

An analysis in the CR3BP proves as useful approach to study the problem in a more general manner. Therefore, in Sections 2.3, 2.4, and 2.5, trajectories are designed first in the CR3BP from halo orbits around L1 and L2, which allows for the identification of reachable asteroids, and provides insight into the ΔV and TOF requirements along the halo orbits. Once trajectories are designed in the CR3BP, they are also computed in an

ephemeris model, where departure points along the CR3BP halo orbit are expressed in the inertial reference frame through Eqs. (4) and (6). Then ephemeris trajectories with the same TOF as those in the CR3BP are computed, in order to see the effect of employing a more realistic dynamical model on the ΔV requirements. Such an approach is used to verify that trajectories computed in the CR3BP also exist in more realistic dynamical models, and to understand whether conclusions drawn from the CR3BP analysis also apply in an ephemeris model.

*2.3. Low-ΔV impulsive trajectory design*

Similarly to the trajectory design problem faced at the end of Chang'e-2's primary mission [31], the goal in the current section is to design impulsive asteroid flyby trajectories departing from a periodic orbit around the Sun-Earth Lagrange points. Such trajectories are designed in such a way that one or two maneuvers allow a spacecraft to intersect the trajectory of an asteroid passing near the Earth.

Potential targets are first identified by understanding how far from the departure L1 and L2 halo orbits a CubeSat could travel with 80 m/s of ΔV. The region that can reached by a CubeSat is approximated in this work leveraging the concept of unstable invariant manifolds associated to the departure halo orbits in the CR3BP model. The unstable direction (away from the Earth-Moon system) associated to points along the departure halo orbits provide the most favorable direction to travel long distances and naturally drift away from the periodic orbit at virtually no cost. Trajectories on the unstable invariant manifolds towards the Earth-Moon system, however, are likely to get trapped by the Earth-Moon gravitational field and are not considered in this study.

In order to approximate the region that can be reached by a CubeSat within 150 days and with 80 m/s of ΔV, a single 80-m/s ΔV maneuver is then implemented along the unstable direction associated to the points on the departure halo orbits, and trajectories are propagated for 150 days. Although these trajectories do not belong to the unstable invariant manifolds in a strictly mathematical sense, their dynamics and behavior are very similar and provide insight into the region that can be reached under the specifications of this mission concept study.

Once the reachable regions from L1 and L2 halo orbits are approximated, the second step is to identify near-Earth asteroids that pass close to these regions and could become potential targets for a mission. In this work, potential targets are selected by: (1) identifying asteroids larger than ~100 meters in diameter (i.e., absolute magnitude <22.5) that pass within 0.1 AU (astronomical unit) from the Earth in years 2019–2025 (this is done through JPL's Center for Near Earth Object Studies [32]), (2) automatedly downloading ephemeris data for those asteroids through JPL's HORIZONS telnet interface [33], and (3) selecting only asteroids whose trajectories pass within 0.01 AU from the reachable regions. Through this pruning process, approximately 40 asteroids are identified as potential targets and are further considered for the design of flyby trajectories.

In particular, asteroid flyby trajectories are designed from nine departure points along the halo orbits (equally spread over one period) in order to provide some insight into the ΔV and time of flight (TOF) requirements along the departure orbits.

The objective of the trajectory optimization process is to minimize the ΔV required to flyby a target asteroid, and the problem is approached using a genetic algorithm in combination with a state-transition matrix differential corrector (embedded within the genetic algorithm).

Because trajectories with one or two impulsive maneuvers are considered, the genetic algorithm is used to optimize two quantities so that the total ΔV requirement is minimized: (1) the ΔV available for the first maneuver (the remaining ΔV becomes available for the second maneuver), and (2) the time after departure at which the second maneuver is executed.

As described in Sections 2.1 and 2.2, the STM can be used to estimate the required change in the initial state (in this case, change in the initial velocity) to satisfy some final conditions (e.g., final position must coincide with the target point). Therefore, for each maneuver, the differential corrector is used to estimate the required ΔV to arrive to the desired encounter point. However, if the required ΔV exceeds the available ΔV for that maneuver, the differential corrector estimates the direction of the maneuver instead (with magnitude equal to the available ΔV) to minimize the distance between the final position and the target. And if the first maneuver already allows the CubeSat to intersect the trajectory of the asteroid from the departure periodic orbit (at a lower cost than a two-maneuver trajectory), then the second maneuver is not implemented.

The STM is effectively defined as the partial derivatives of the final state with respect to the initial state, as represented in Eq. (8):

$$\Phi(t_f, t_0) = \begin{bmatrix} \dfrac{\delta \bar{r}(t_f)}{\delta \bar{r}(t_0)}, & \dfrac{\delta \bar{r}(t_f)}{\delta \bar{v}(t_0)} \\ \dfrac{\delta \bar{v}(t_f)}{\delta \bar{r}(t_0)}, & \dfrac{\delta \bar{v}(t_f)}{\delta \bar{v}(t_0)} \end{bmatrix} \qquad (8)$$

If, for instance, variations in the final position are to be related to variations in the initial velocity, the 3x3 top-right block in the STM is of special interest (see Eq. (9)).

$$\frac{\delta \bar{r}(t_f)}{\delta \bar{v}(t_0)} = \begin{bmatrix} \frac{\delta x(t_f)}{\delta \bar{v}(t_0)} \\ \frac{\delta y(t_f)}{\delta \bar{v}(t_0)} \\ \frac{\delta z(t_f)}{\delta \bar{v}(t_0)} \end{bmatrix} = \begin{bmatrix} \frac{\delta x(t_f)}{\delta v_x(t_0)} & \frac{\delta x(t_f)}{\delta v_y(t_0)} & \frac{\delta x(t_f)}{\delta v_z(t_0)} \\ \frac{\delta y(t_f)}{\delta v_x(t_0)} & \frac{\delta y(t_f)}{\delta v_y(t_0)} & \frac{\delta y(t_f)}{\delta v_z(t_0)} \\ \frac{\delta z(t_f)}{\delta v_x(t_0)} & \frac{\delta z(t_f)}{\delta v_y(t_0)} & \frac{\delta z(t_f)}{\delta v_z(t_0)} \end{bmatrix} \quad (9)$$

which can be used to estimate the initial ΔV (direction and magnitude) required to achieve a desired final condition. If the required ΔV, however, exceeds the available ΔV for a maneuver (provided by the genetic algorithm), the STM can also be used to estimate only the direction of the required ΔV. For such purpose, the initial velocity can be expressed (see Eq. (10)) in terms of its norm, $|\bar{v}(t_0)|$, and two angles representing its direction, for instance, $\varepsilon$ and $\theta$ (elevation with respect to the Sun-EMB plane, and in-plane azimuth):

$$\bar{v}(t_0) = |\bar{v}(t_0)| \cdot \begin{bmatrix} \cos(\varepsilon(t_0)) \cdot \cos(\theta(t_0)) \\ \cos(\varepsilon(t_0)) \cdot \sin(\theta(t_0)) \\ \sin(\varepsilon(t_0)) \end{bmatrix} \quad (10)$$

As an example, the variation in the final $x$-component, $\delta x(t_f)$, can then be related to variations in the two angles by taking the partial derivatives of the initial velocity with respect to $\varepsilon$ and $\theta$, and by applying the chain rule to Eq. (9):

$$\frac{\delta x(t_f)}{\delta \varepsilon(t_0)} = \frac{\delta x(t_f)}{\delta \bar{v}(t_0)} \cdot \frac{\delta \bar{v}(t_0)}{\delta \varepsilon(t_0)} \qquad \frac{\delta x(t_f)}{\delta \theta(t_0)} = \frac{\delta x(t_f)}{\delta \bar{v}(t_0)} \cdot \frac{\delta \bar{v}(t_0)}{\delta \theta(t_0)} \quad (11)$$

In this way, the components of the STM can be transformed to lastly relate variations in the final state due to variations in the initial direction of the velocity.

The initial guess for the trajectory optimization algorithm is a single-maneuver, 150-day trajectory with a departure maneuver of 80 m/s in the unstable direction, and each iteration in the trajectory optimization algorithm is composed of the following steps: (1) genetic algorithm provides values for the maximum magnitude of the first maneuver and time of the second maneuver, (2) retrieve previous guess for first maneuver, limit its magnitude, and propagate trajectory for 150 days, (3) identify closest point on the trajectory of the asteroid to the propagated trajectory, and update the target point with this closest point, (4) use STM differential corrector to iteratively compute the ΔV that will minimize the distance to the updated target point (considering its limited magnitude), propagate trajectory with new ΔV for 150 days, and compute minimum distance to the trajectory of the asteroid. If the distance between both trajectories is below a convergence threshold, only one maneuver is necessary and thus proceed with step (6); if not, second maneuver is required and thus proceed with step (5): (5) retrieve previous guess for second maneuver, limit its magnitude, implement maneuver at the time of the second maneuver, and propagate until total trajectory spans 150 days. Repeat steps (3) and (4) for second impulsive maneuver. And (6) store total ΔV and minimum distance to the trajectory of the asteroid, and then proceed with next iteration.

Finally, it is worth clarifying that trajectories are designed to flyby the asteroids on their illuminated face (for proper visibility of the asteroid during the flyby). Specifically, the trajectory optimization algorithm targets points 1000 kilometers from the trajectory of the asteroid, along the lines connecting each point on the trajectory of the asteroid to the Sun.

Such a trajectory optimization process is employed for the computation of impulsive asteroid flyby trajectories in the CR3BP model, and allows for the identification of reachable near-Earth asteroids under the constraints of 80-m/s ΔV and 150-day TOF.

The same logic is then used for the design of flyby trajectories in an ephemeris model, to verify similar trajectories also appear in a more realistic dynamical model (i.e., genetic algorithm plus differential corrector, but now subject to the ephemeris dynamical model in Eq. (7)). In this work, however, ephemeris trajectories are only computed for those asteroids that are first reachable in the CR3BP, and from the same departure points. The departure conditions along the CR3BP halo orbits are expressed in the inertial reference frame at the departure time associated to the CR3BP solution (as described in Section 2.2). For example, if an asteroid can be reached in the CR3BP at 12:00AM on December 31st, 2019, and the TOF is 30 days, then the synodic position and velocity of that departure point are expressed in the inertial reference frame at 12:00AM on December 1st, 2019. From those departure conditions, flyby trajectories are computed in the ephemeris model with appropriate correspondence between the TOF and the position of the asteroid along time.

Results for this section can be found in Section 4.1.

### *2.4. High-fidelity quasi-impulsive trajectory refinement*

Once impulsive trajectories are designed in the CR3BP, equivalent trajectories are computed using a more realistic thruster model. Thruster specifications are drawn from those of VACCO's 0.5U PUC [34], whose nominal thrust is 5 mN, the total ΔV is approximately 80 m/s, and it requires a 20-minute-on/20-minute-off duty

cycle for temperature control (D. Carroll at CU Aerospace, personal communication, April 23, 2018).

The highest fidelity quasi-impulsive model considered in this work is such that each impulsive maneuver is modeled as multiple 20-minute continuous and constant thrust arcs instead, with 20 minutes in between arcs where the thruster is off. Each arc should also have a thrust magnitude of at most 5 mN, continuously exerted over the span of 20 minutes. For simplicity in the modelization of the thrust arcs, an additional constraint is imposed on the thrust such that each 20-min thrust arc should have a constant direction and magnitude in the CR3BP synodic reference frame. In addition, two intermediate models are also developed to transition from the impulsive-maneuver model to the highest-fidelity quasi-impulsive model.

In increasing order of fidelity, the first model considered is such that each impulsive maneuver is modeled as multiple smaller impulsive maneuvers (40 minutes apart from each other) of equivalent cumulative ΔV. In this model, the one or two impulsive trajectories described in Section 2.3 are used as reference. Because the nominal thrust magnitude is 5 mN, the ΔV that can be exerted over 20 minutes, $\Delta V_{20\,min}$, is $\Delta V_{20\,min} = (0.005\ N)\cdot(20\ min)\cdot(60\ s/min)/(4\ kg) = 1.5\ m/s$ (for a 4-kg, 3U CubeSat). Consequently, if, for example, two impulsive maneuvers of 15 m/s and 45 m/s were required to reach an asteroid, now these two maneuvers are modeled as $(15\ m/s)/(1.5\ m/s) + 2 = 12$ and $(45\ m/s)/(1.5\ m/s) + 2 = 32$ small maneuvers instead, each of which at most 1.5 m/s in magnitude. The first 12 maneuvers are executed starting at time $t = 0$ (40 minutes apart from each other), and then half of the remaining 32 maneuvers are placed before the second original maneuver, and the other half are executed after the second original maneuver. Also notice that two additional 1.5-m/s maneuvers are allocated for each original maneuver in order to facilitate the convergence properties of the refinement algorithm (adding specifically two 1.5-m/s maneuvers showed good convergence properties in this analysis). Finally, the direction and magnitude of each 1.5-m/s maneuver is determined using the STM single-shooting method described in Section 2.1, with the goal of shadowing the reference trajectory (i.e., impulsive trajectory) and arriving to the same asteroid encounter point.

The second model of increasing order of fidelity uses the trajectory obtained in the first intermediate model as reference, and now each 1.5-m/s maneuver is modeled as three equal maneuvers of at most 0.5 m/s in magnitude instead, all three with the same direction and magnitude. These 0.5-m/s maneuvers are executed within 20 minutes past the time of the associated 1.5-m/s maneuver, in intervals of 10 minutes: i.e., effectively modelling a 20-min continuous thrust maneuver as three equal 0.5-m/s maneuvers, with one 0.5-m/s maneuver at the beginning of the 20 minutes, one in the middle, and one at the end. Each set of three 0.5-m/s maneuvers is then followed by a 20-minute coast (i.e., thruster is off). Again, the direction and magnitude of each set of three 0.5-m/s maneuvers are determined through an STM single-shooting method, with the goal of shadowing the reference trajectory (i.e., first intermediate model).

Because the trajectories considered in the second intermediate model include three impulsive maneuvers along the trajectory, the STM from time $t_0$ to time $t_f$ is not propagated through Eq. (2) (which does not include the effect of maneuvers throughout the trajectory), but it is found numerically [35]. The $i$-th row and $(j+3)$-rd column component of the STM, $\Phi(t_f, t_0)_{i,(j+3)}$, is found in this case according to Eq. (12):

$$\Phi(t_f, t_0)_{i,(j+3)} = \frac{\bar{x}^S(t_f; \delta v_j^+)_i - \bar{x}^S(t_f; \delta v_j^-)_i}{2\cdot|\delta v_j|} \tag{12}$$

where $\bar{x}^S(t_f; \delta v_j^+)_i$ and $\bar{x}^S(t_f; \delta v_j^-)_i$ are the $i$-th component of the state vector $\bar{x}^S$ resulting from the propagation of the trajectory from time $t_0$ to time $t_f$ with three (small and equal) impulsive maneuvers ($\delta v_j^+$ and $\delta v_j^-$) along the positive and negative $j$-th component of the velocity, executed at times $t_0$, $(t_0 + 10\ min)$, and $(t_0 + 20\ min)$. This computation of the STM allows to estimate the set of three equal 0.5-m/s maneuvers required to achieve a desired final state.

Finally, the highest-fidelity quasi-impulsive model considered in this work uses the second intermediate model as a reference, and now maneuvers are modeled as 20-min continuous and constant thrust arcs of at most 5 mN in magnitude, exerted in a fixed direction in the CR3BP synodic reference frame. Each thrust arc is initiated at the time of the 1.5-m/s maneuvers in the first intermediate model, and a continuous thrust force is then exerted over the span of 20 minutes. The constant direction and magnitude of each thrust arc are also determined through an STM differential corrector, but the equations of motion are modified to include the effect of the thrust. The EoM describing the dynamics of spacecraft during a thrusting arc are summarized in Eq. (13):

$$\begin{aligned}\frac{dv_x^S}{d\tilde{t}} = \frac{d^2x^S}{d\tilde{t}^2} &= -(1-\mu)\frac{(x^S+\mu)}{d^3} - \mu\frac{(x^S-1+\mu)}{r^3} + x^S + 2v_y^S + T_x^S/m \\ \frac{dv_y^S}{d\tilde{t}} = \frac{d^2y^S}{d\tilde{t}^2} &= -(1-\mu)\frac{y^S}{d^3} - \mu\frac{y^S}{r^3} + y^S - 2v_x^S + T_y^S/m\end{aligned} \tag{13}$$

$$\frac{dv_z^S}{d\tilde{t}} = \frac{d^2 z^S}{d\tilde{t}^2} = -(1-\mu)\frac{z^S}{d^3} - \mu\frac{z^S}{r^3} + T_z^S/m$$

$$\frac{dm}{d\tilde{t}} = -\frac{|\bar{T}^S|}{I_{sp}\cdot g_0}$$

where $\bar{T}^S = \left(T_x^S, T_y^S, T_z^S\right)^T$ is the thrust vector expressed in the non-dimensional synodic reference frame, $m$ is the mass of the spacecraft, and $I_{sp}$ and $g_0$ are the non-dimensional specific impulse of the thruster and gravitational acceleration at sea level, respectively. Notice that this is the first time the change in the mass of the spacecraft is considered in the EoM: until now, the mass of the spacecraft was considered constant and equal to 4 kg throughout the whole trajectory.

As described in Eq. (3), the STM relates variations in the final state due to variations in the initial state. Because the STM is to be used now to estimate the thrust vector required to achieve a desired final state, the STM should be modified to include information on the final variations due to variations in the thrust vector. With such a purpose, the state vector is extended to include not only position and velocity coordinates and the mass of the spacecraft, but also the thrust components. The extended state vector (expressed in the synodic reference frame) is therefore defined as $\bar{X}^S = \left(x^S, y^S, z^S, v_x^S, v_y^S, v_z^S, m, T_x^S, T_y^S, T_z^S\right)^T$, and the EoM are also extended with the differential equations for the thrust components (constant throughout each thrust arc):

$$\frac{dT_x^S}{d\tilde{t}} = \frac{dT_y^S}{d\tilde{t}} = \frac{dT_z^S}{d\tilde{t}} = 0 \qquad (14)$$

As usual, the STM is defined as the partial derivatives of the (now extended) EoM (i.e., Eqs. (13) and (14)) with respect to the (now extended) state vector. In such a way, variations in the final state at the end of a thrust arc can be related to changes in the thrust components exerted during the arc (and during a coasting arc, the non-extended state vector and STM are propagated according to the dynamics in Eq. (1)). This methodology is used to determine the direction and magnitude of each constant and continuous 20-min thrust arc, with the goal of shadowing the reference trajectory (i.e., second intermediate model).

Results for this section can be found in Section 4.2.

### *2.5. Low-thrust trajectory design*

In contrast to the impulsive and quasi-impulsive trajectories computed in Section 2.3, in which the thruster generated an (almost) instantaneous change in velocity, low-thrust trajectories are such that the thruster exerts a continuous force over an extended period of time, which may not negligible in comparison to the overall timespan of the mission.

In this work, low-thrust trajectories are generated through a two-step process: (1) an initial guess for the trajectory is generated using a genetic algorithm in combination with a state-transition matrix differential corrector, and (2) the initial guess is provided to a direct optimization solver to refine the solution.

For the initial guess, trajectories with one or two continuous thrust arcs are considered, and the thrust arcs are also constrained to have a constant magnitude and fixed direction throughout the arc (such as the quasi-impulsive trajectories in Section 2.4). The genetic algorithm is in this case employed to determine three quantities in search of a minimum total ΔV: (1) the duration of the thrust arc, (2) the starting time of the second thrust arc, and (3) the duration of the second thrust arc. The magnitude of the thrust arcs is constrained to be equal to the maximum thrust magnitude available from the thruster: Busek's electrospray BET-100 propulsion system has a maximum thrust magnitude of 100 μN.

Within each iteration of the genetic algorithm, an STM differential corrector is embedded to determine the required direction and magnitude of each thrust arc. The logic used within each iteration of the optimization process is exactly the same as that described in Section 2.3, but in this case, the problem deals with thrust arcs instead of impulsive maneuvers.

The dynamics used for the propagation of the trajectory and STM during continuous thrust arcs are those previously summarized in Eqs. (13) and (14) (which consider the extended state vector $\bar{X}^S$), and when the thruster is off, the trajectory and STM are propagated according to the unpowered EoM in Eq. (1).

If the trajectory optimization algorithm is able to find flyby trajectories of less than 80 m/s, then those solutions are provided as the initial guess to a direct optimization solver to refine the solution [36]. In specific, a Gaussian pseudospectral method is used to: (1) discretize the trajectory into segments (bounded by nodes), (2) approximate the states and controls (i.e., generated thrust) between nodes via Lagrange interpolating polynomials, (3) transcribe the equations of the optimal control problem into a nonlinear programming (NLP) problem, and (4) solve the NLP problem.

The direct optimization solver thus provides a discretized solution for the optimal control problem, in which the thrust magnitude and direction throughout the trajectory are refined and are no longer constrained to have a constant magnitude or a fixed direction.

Results for this section can be found in Section 4.3.

## 3. Autonomous navigation and sensitivity analysis

Once low-energy flyby trajectories are designed to identify potential asteroid exploration opportunities despite the limited propulsive capabilities of CubeSats, it is also of interest to understand whether a CubeSat could autonomously estimate its own trajectory and correct it

despite the limited number of sensors and actuators on board and their limited performance.

In this work, this navigation and sensitivity analysis is only performed for the impulsive flyby trajectories designed in Section 2.3, and the CubeSat is assumed to be equipped with the following components relevant to the analysis: (1) VACCO's 0.5U Propulsion Unit for CubeSats [19], (2) Blue Canyon Technologies' (BCT's) 0.5U XACT ADCS (attitude determination and control system) [37], (3) PROBA-2's 0.125U star tracker [38], substituting the 0.125U star tracker originally integrated within the XACT ADCS unit (for earlier detection of the target asteroid—see Section 4.4), and (4) a coarse sun sensor (either the one already integrated in the XACT ADCS unit [39], or an off-the-shelf component [40]).

The performance of these components is summarized in Table 1. These values are representative of the current state of CubeSat technology and are used to model errors in Monte Carlo simulations.

A simple autonomous navigation strategy is considered in this analysis, in which only two kinds of observations are collected by the CubeSat: (1) coarse sun sensor observations of the Sun during cruise, and (2) navcam observations of the target asteroid prior to the flyby. The navigation camera considered in this work is the star tracker integrated within the ADCS unit, although other alternatives might exist (e.g., redundant star tracker, optical camera within science payload, etc.).

Through the sun sensor, measurements of the direction from the CubeSat to the Sun can be collected. Observations are collected every hour once the CubeSat has executed the one or two maneuvers required to reach the asteroid (i.e., during cruise). Once the asteroid becomes visible by the navcam, observations of the target asteroid are collected instead. These observations are collected every hour as well, and provide a measurement of the direction from the CubeSat to the asteroid (of known trajectory), and an estimation of the distance from the CubeSat to the asteroid (e.g., through pixel brightness). Pixel brightness could be related to the apparent visual magnitude of the asteroid as viewed from the CubeSat, and this magnitude is directly related to their relative distance [42,43]. Because measurements of the asteroid's apparent magnitude are likely to contain high levels of uncertainty, a conservative 30% 3σ error is assumed in the observations.

These observations are then processed by a non-linear least squares estimator [44], to estimate the trajectory of the CubeSat (position and velocity). Due to the errors introduced by the components of the CubeSat (e.g., errors in the impulsive maneuvers and uncertainties in the observations), an impulsive trajectory correction maneuver (TCM) becomes necessary to achieve an asteroid flyby of reasonable accuracy (for significant scientific return). The TCM is computed through an STM single-shooting and using the trajectory estimation provided by the least squares estimator, with the goal of achieving an asteroid flyby with the same conditions as those in the nominal, unperturbed trajectory (same position and same time).

Table 1. On-board component performance

| Parameter | Value | Reference |
|---|---|---|
| ΔV magnitude accuracy (3σ) | 1% | VACCO's 0.25U PUC, <5% magnitude uncertainty[a] [19] |
| ADCS pointing accuracy (3σ) | ±0.02 deg | BCT's 0.5U XACT unit, ±0.02-deg boresight pointing accuracy[b] [41] |
| ADCS pointing knowledge (3σ) | ±0.01 deg | PROBA-2's star tracker, ±0.0006-deg pointing knowledge [38] |
| Sun sensor pointing knowledge (3σ) | ±1 deg | Hyperion Technologies' sun sensor, <1-deg pointing knowledge [40] |

[a] Magnitude uncertainty includes experimental measurement error.

[b] Cross-axis pointing accuracy is two to three times better than boresight performance.

The goal of this analysis is to understand the flyby accuracies that can achieved through this simple navigation strategy, and according to the current state of CubeSat technology (Table 1). Monte Carlo simulations are performed by introducing normally-distributed errors in the following elements: (1) departure conditions from halo orbit (3σ uncertainty of 10 km in position and 0.1 m/s in velocity), (2) direction and magnitude of all impulsive maneuvers (i.e., nominal maneuvers and TCM, 0.02-deg and 1% 3σ errors), (3) direction from the CubeSat to the Sun from sun sensor measurements (1-deg 3σ error), (4) direction from the CubeSat to the asteroid from navcam measurements (0.01-deg 3σ error), and (5) apparent visual magnitude of the asteroid from navcam measurements, which provide information on the relative distance to the asteroid (30% 3σ error).

Errors not considered in this analysis, however, primarily include: (1) uncertainties in the trajectory of the target asteroid, and (2) errors introduced because the on-board least squares estimator and STM shooting algorithm use a dynamical model that does not perfectly represent the real dynamics of the system. In this study, the real dynamics are assumed to be those of the CR3BP, and the on-board algorithms for the trajectory estimation and maneuver computation also use the CR3BP dynamics; in a real mission, however, the real dynamics are those of a full-ephemeris $n$-body problem (plus non-

gravitational effects), and the on-board algorithms will generally use a lower fidelity dynamical model.

Additionally, the timing of the TCM will also have an effect on the resulting flyby accuracies, and this is also analyzed in the Monte Carlo simulations. Two competing factors should be considered: (1) the later the TCM is executed, the more observations can be collected and therefore the better the trajectory estimation, and (2) the later the TCM is executed, the higher the ΔV requirement to correct the trajectory of the CubeSat. Properly timing the TCM is therefore crucial for the accuracy of the flyby. Monte Carlo simulations are thus performed for TCM execution times every 0.5 days once the asteroid becomes visible by the on-board navigation camera. For instance, if an asteroid becomes visible by the navcam 3.2 days before the flyby, Monte Carlo simulations are performed for the cases in which the TCM is executed at time 3.0 days before the flyby, at time 2.5 days before the flyby, at time 2.0 days before the flyby, and so on.

One thousand Monte Carlo simulations are performed for each TCM execution time, for all departure points along the halo orbit from which the target asteroid can be reached with less than 60 m/s of ΔV (in order to allocate at less 20 m/s of ΔV for the TCM).

Results for this section can be found in Section 4.4.

## 4. Results and discussion

Potential targets for asteroid flyby missions are identified through the pruning process described in Section 2.3, which uses the CR3BP as reference dynamical model, and a single 80-m/s impulsive maneuver to depart from the halo orbits. For the time window between years 2019 and 2025, approximately 40 potential targets are identified.

In Fig. 1, the approximate regions that can be reached by a CubeSat from the Sun-EMB L1 and L2 points are illustrated (with 80 m/s of ΔV and within 150 days), along with potential targets whose trajectories pass close to the reachable regions (represented in the non-dimensional Sun-EMB synodic reference frame).

### *4.1. Low-ΔV impulsive trajectory design*

Impulsive trajectories with one or two maneuvers are designed in the CR3BP as described in Section 2.3, from nine points along the departure halo orbits.

Asteroid 2016 CZ31, for instance, has a close encounter with Earth on July 29, 2022, and it can be reached from L1 from seven out of the nine points considered. Requirements in ΔV and TOF along the departure halo orbit are illustrated in Fig. 2 (in the Sun-EMB synodic reference frame).

At least 24 asteroids are identified to be reachable from L1 and L2 between 2019 and 2025. For each of those asteroids, Table 2 summarizes the range of ΔV requirements and TOFs along the departure halo orbits.

It is therefore observed that multiple asteroid flyby opportunities are available within the 2019–2025 time window (in average ~4 opportunities per year), with ΔV requirements as low as 3.4 m/s; although these are highly dependent on the departure point from the halo orbit.

In order to verify the trajectories computed in the CR3BP also appear in higher-fidelity dynamical models, trajectories are also designed in an ephemeris model (as described in Section 2.3). For comparison with Fig. 2, ΔV requirements and TOFs to reach asteroid 2016 CZ31 in an ephemeris model are summarized in Fig. 3, and the resulting trajectories in the two models (from one departure point in the halo orbit) are illustrated in Fig. 4.

It is observed in Fig. 3 that trajectories in the ephemeris model have significantly higher ΔV requirements than in the CR3BP; however, flyby trajectories still exist and with ΔV costs well within the 80-m/s constraint. In a geometrical sense, Fig. 4 illustrates how trajectories in the two models follow a similar behavior. In order to obtain more accurate estimates of the costs in the high-fidelity ephemeris model, it might be advisable to perform the preliminary analysis in the elliptic restricted three-body problem instead of the CR3BP.

### *4.2. High-fidelity quasi-impulsive trajectory refinement*

Once impulsive trajectories are designed, trajectories with a higher-fidelity thruster model are also computed.

The ultimate goal of the three-step refinement process described in Section 2.4 is to model propulsive maneuvers as 20-min-on/20-min-off thruster arcs (instead of as impulsive maneuvers). The nominal thrust of VACCO's 0.5U PUC is 5 mN, and its specific impulse is 70 seconds [19]. As an example, ΔV requirements and TOFs to reach asteroid 2016 CZ31 from L1 for this thruster model are illustrated in Fig. 5. For comparison, Fig. 2 summarized these requirements using an impulsive-maneuver model instead.

It is observed that the agreement in terms of ΔV requirements and TOFs between the impulsive-maneuver model and the 20-min continuous thrust model is well within 10%. Through the refinement process in Section 2.4, therefore, equivalent trajectories to those computed in Section 4.1 can be obtained, but using a more realistic thruster model instead (no apparent visual difference between the trajectories can be observed either). It can also be concluded that the impulsive-maneuver model can serve as a good first approximation to estimate ΔV requirements and TOFs, despite the long times required by the thruster to generate the total ΔV.

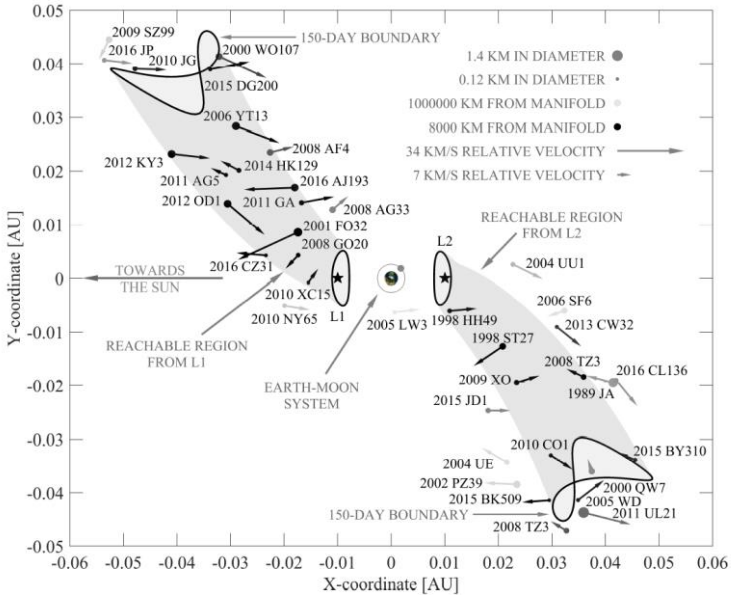


Fig. 1. Reachable regions from Sun-EMB L1 and L2 points and potential targets

Table 2. ΔV and TOF requirements for reachable asteroids (CR3BP, impulsive maneuvers)

| Asteroid | From | ΔV range | TOF range |
|---|---|---|---|
| 2013 CW32 | | 64.6↔76.0 | 137.6↔150.0 |
| 2010 CO1 | | 64.1↔68.6 | 135.7↔150.0 |
| 2000 QW7[a] | | 45.5 | 138.0 |
| 2005 WD[a] | | 73.5 | 136.3 |
| 2015 BK509 | | 48.8 | 150.0 |
| 2009 XO | L2 | 17.4↔74.7 | 104.4↔150.0 |
| 2008 TZ3 | | 22.5↔80.0 | 107.1↔150.0 |
| 2015 BY310[a,b] | | 61.0 | 143.6 |
| 2015 BY310[a,b] | | 53.4 | 150.0 |
| 1998 HH49 | | 11.3↔64.5 | 66.7↔150.0 |
| 1998 ST27 | | 13.4↔69.5 | 100.0↔149.8 |
| 2010 JG | | 45.2↔61.7 | 137.5↔144.7 |
| 2001 FO32 | | 3.4↔69.4 | 76.1↔150.0 |
| 2008 GO20 | | 6.1↔70.3 | 73.1↔150.0 |
| 2016 AJ193 | | 12.3↔71.9 | 105.2↔144.0 |
| 2006 YT13 | | 28.7↔73.2 | 119.5↔150.0 |
| 2016 CZ31 | | 4.3↔57.0 | 88.9↔150.0 |
| 2014 HK129 | L1 | 21.8↔52.9 | 126.6↔150.0 |
| 2010 XC15 | | 2.3↔70.9 | 73.9↔150.0 |
| 2015 DG200 | | 33.9↔70.4 | 129.7↔150.0 |
| 2011 AG5 | | 8.6↔66.7 | 88.2↔143.5 |
| 2012 KY3 | | 30.3↔70.4 | 121.9↔150.0 |
| 2009 SZ99[a] | | 67.9 | 140.6 |
| 2011 GA | | 9.3↔61.8 | 107.6↔150.0 |
| 2012 OD1 | | 12.2↔66.5 | 105.9↔150.0 |

[a] Reachable from only one out of the nine departure points considered.

[b] Asteroid 2015 BY310 can be reached from L2 in 2021 and 2023.

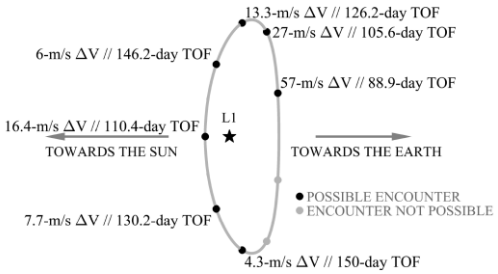


Fig. 2. ΔV and TOF requirements for asteroid 2016 CZ31 from L1 (CR3BP, impulsive maneuvers)

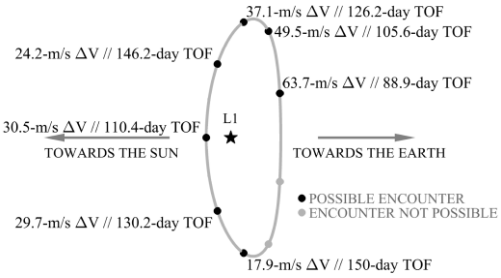


Fig. 3. ΔV and TOF requirements for asteroid 2016 CZ31 from L1 (ephemeris, impulsive maneuvers)

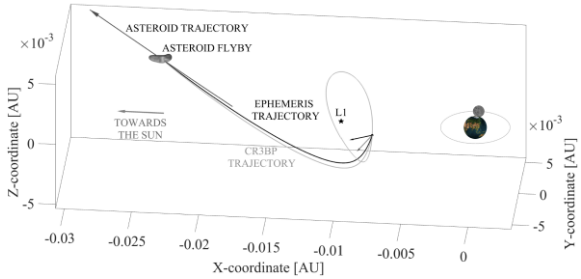


Fig. 4. 2016 CZ31 encounter trajectory in CR3BP and ephemeris models (impulsive maneuvers)

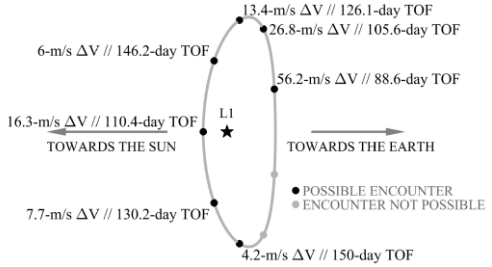


Fig. 5. ΔV and TOF requirements for asteroid 2016 CZ31 from L1 (CR3BP, high-fidelity thruster model)

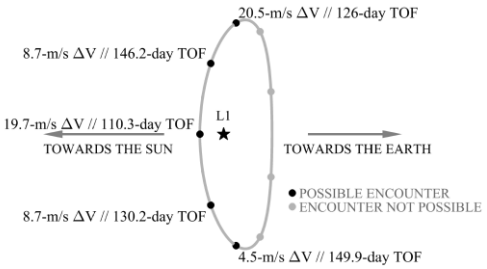


Fig. 6. ΔV and TOF requirements for asteroid 2016 CZ31 from L1 (CR3BP, low thrust)

It is also worth mentioning that in terms of efficiency, impulsive-maneuver trajectories should have lower ΔV requirements than quasi-impulsive trajectories. However, it is also observed that for departure points with large ΔV requirements (e.g., right-most departure point in Fig. 2 and Fig. 5), a more realistic thruster model might result in lower ΔV requirements instead—this is because the dynamical model considered for the quasi-impulsive trajectories includes variations in mass throughout the trajectory (which divides the thrust components in Eq. (13)), whereas impulsive trajectories were computed in terms of ΔV (regardless of the mass) and not in terms of thrust.

*4.3. Low-thrust trajectory design*

Following the low-thrust trajectory design process described in Section 2.5, trajectories are computed using Busek's 100-μN BET-100 thruster, whose specific impulse is 2300 seconds [20].

Using the same asteroid as an example, Fig. 6 summarizes low-thrust ΔV requirements and TOFs to reach asteroid 2016 CZ31 from L1. As a general trend, low-thrust ΔV requirements are anywhere between 10% and 50% higher than for impulsive trajectories, due to the long times required to generate the total ΔV (no significant visual difference between the low-thrust and impulsive trajectories is observed).

Additionally, it is noted that through the trajectory design process in Section 2.5 (i.e., initial guess plus direct optimization solver), low-thrust trajectories from certain departure points cannot be found, even though impulsive trajectories were computed from these points (e.g., top-right points in Fig. 6 and Fig. 2). Low-thrust trajectories have generally higher ΔV requirements than impulsive trajectories, and it is therefore logical that asteroids can be reached from fewer departure points along the halo orbits. However, it is also possible that low-thrust trajectories actually exist from some of these points, but an initial guess for these flyby trajectories cannot be constructed via the simple thrusting strategy considered in Section 2.5 (i.e., one or two fixed-direction and constant-magnitude thrust arcs). For a more thorough analysis of low-thrust ΔV requirements along the halo orbits, a more complex thrusting strategy for the initial guess may be required (e.g., thrust arcs of linearly- or quadratically-varying direction).

As an example of how the direct optimization solver refines the initial guess, Fig. 7 illustrates the history of the thrust magnitude (in the initial guess and in the optimal solution) associated to the left-most departure point in Fig. 6:

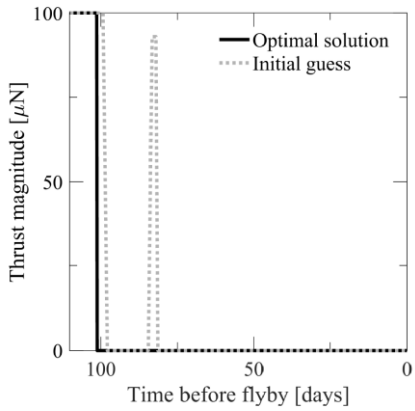


Fig. 7. Initial guess and optimal thrust history

In Fig. 7, it is observed how the initial guess (dotted line) is constructed using two thrust arcs along the trajectory (which last approximately 10 days and 1.5 days). The optimal solution found by the optimizer (solid line), however, is composed of only one thrust arc, and this thrust arc is also shorter than the initial maneuver of the initial guess. As a result, the ΔV of the initial guess (~30 m/s) is reduced down to 19.7 m/s (as shown in Fig. 6). In addition to optimizing the thrust magnitude, the direct optimization solver also refines the direction of the thrust throughout each thrust arc.

*4.4. Autonomous navigation and sensitivity analysis*

The autonomous navigation strategy described in Section 3 is applied to the CR3BP impulsive trajectories computed in Section 4.1 .

Such navigation strategy employs observations of the asteroid once it becomes visible by the navigation camera. Detecting the asteroid sufficiently early, therefore, will strongly influence the accuracy of the trajectory estimation. Monte Carlo simulations are thus

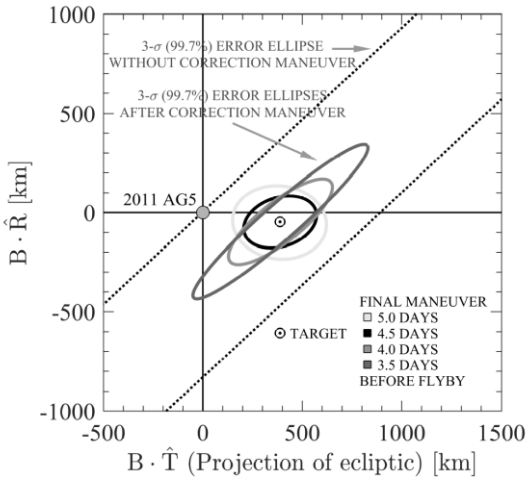


Fig. 8. 3σ error ellipses for asteroid 2011 AG5 from L1 (CR3BP, impulsive maneuvers)

performed only for asteroids that are visible for at least 3 days before the flyby. In addition, and as mentioned in Section 3, simulations are also performed only for those asteroids that can be reached with at least 20 m/s of ΔV still remaining for the trajectory correction maneuver.

The constraints in asteroid visibility time and ΔV available for the TCM further limit the number of autonomously reachable asteroids. Considering a detectability threshold in apparent visual magnitude of 15 (determined by the capabilities of the navcam, e.g., PROBA-2's star tracker [45]), the number of asteroids fulfilling these two constraints is nine (out of the 25 opportunities summarized in Table 2). Alternative autonomous navigation strategies that do not largely depend on observations of target asteroid may not so severely limit the number of autonomous flyby opportunities (e.g., collecting observations of other large planetary bodies instead [46]).

Asteroid 2011 AG5, for instance, is visible for 5.3 days before the flyby, and can be reached from L1 with 31.1 m/s of ΔV (from one of the departure points). As described in Section 3, Monte Carlo simulations are performed for TCM execution times every 0.5 days (at 5.0 days before the flyby, 4.5 days before the flyby, etc.). The B-plane 3σ error ellipses resulting from these TCM execution times are illustrated in Fig. 8. It is observed how the execution time of the TCM greatly influences the size and orientation of the error ellipses: if the TCM is executed 4.5 days before the flyby, the best-case error ellipse is obtained (±155 km error ellipse); if the TCM is executed 5.0 days before the flyby, not enough observations of the asteroid have been collected and the estimation error is still large (±240 km error ellipse); and if the TCM is executed less than 4.5 days before the flyby, the ΔV requirement to correct the trajectory increases and the CubeSat is not able to fully correct its trajectory anymore (error ellipses larger than ±240 km).

Table 3. Best-case error ellipses for asteroids flown by autonomously (CR3BP, impulsive maneuvers)

| Asteroid | From | 3σ error ellipse[b] (km) | Visibility time |
|---|---|---|---|
| 2000 QW7[a] | L2 | ±2484 | 8.8 |
| 2008 TZ3 | | ±337↔±1771 | 7.1 |
| 2015 BY310[a] | | ±12657 | 4.9 |
| 1998 ST27 | | ±226↔±851 | 5.3 |
| 2001 FO32 | L1 | ±294↔±9239 | 7.0 |
| 2016 AJ193 | | ±172↔±770 | 6.7 |
| 2014 HK129 | | ±1855↔±7218 | 5.7 |
| 2010 XC15 | | ±137↔±10407 | 3.5 |
| 2011 AG5 | | ±77↔±702 | 5.3 |

[a] Reachable from only one out of the nine departure points considered.

[b] Smallest and largest best-case error ellipses out of all departure points from which asteroid is reachable.

The best-case error ellipse is ±155 km in this case; however, the size of the ellipses is dependent on the departure point. Table 3 summarizes the largest and smallest best-case error ellipses out of all the departure points from which asteroids can be reached autonomously.

Great variability in error ellipse size is observed in Table 3, which is primarily influenced by the time the target asteroid is visible by the on-board navigation camera, and by the ΔV that remains available for the TCM. A flyby accuracy of ±137 km, for instance, can be obtained for asteroid 2010 XC15 when only 2.3 m/s of ΔV where used for the nominal impulsive maneuvers. If less ΔV remains available for the TCM, however, error ellipses as large as ±10,407 km are obtained given the short asteroid visibility time (3.5 days).

## 5. Conclusions

A methodology is presented to design high-fidelity, low-energy asteroid flyby trajectories subject to the stringent propulsive capabilities of CubeSats. Trajectories are computed assuming a deployment around the Sun-Earth Lagrange points, from where a CubeSat could depart and flyby a near-Earth asteroid.

Employing the Circular Restricted Three-Body Problem as reference model, trajectories are computed using impulsive maneuvers, quasi-impulsive maneuvers (i.e., introducing a more realistic thruster model), and low thrust. The cost of low-thrust trajectories is found to be comparable but slightly higher than for impulsive and quasi-impulsive trajectories. The existence of impulsive trajectories in an ephemeris model is also verified. Their cost is found to be significantly higher, but still within the capabilities of current propulsion systems.

In addition, the flyby accuracies that can be achieved through autonomous navigation are assessed via Monte Carlo simulations. Through a simple navigation strategy

(observations of the Sun and of the asteroid), flyby accuracies of the order of one-hundred kilometers are found possible; although these are subject to the available propellant, capabilities of the navigation camera, etc.

Ultimately, this work shows that asteroid flyby missions with relevant scientific return are nowadays possible using CubeSats. Several flyby opportunities between 2019 and 2025 are identified, and simple autonomous navigation strategies are rendered viable.

**References**


[1] A.R. Aslan, H.B. Yağcı, M.E. Umit, A. Sofyalı, M.E. Bas, M.S. Uludag, O.E. Ozen, M.D. Aksulu, E. Yakut, C. Oran, M. Suer, İ.A. Akyol, A.B. Ecevit, M.S. Ersöz, İ. Öz, Ş. Gülgönül, B. Dinç, T. Dengiz, Development of a LEO Communication CubeSat, in: 2013 6th International Conference on Recent Advances in Space Technologies (RAST), 2013: pp. 637–641. doi:10.1109/RAST.2013.6581288.

[2] R. Jove-Casulleras, A. Camps, J. Ramos, Cubesat-based Demonstrator for Optical Earth Observation, in: 2012 IEEE International Geoscience and Remote Sensing Symposium, 2012: pp. 1505–1508. doi:10.1109/IGARSS.2012.6351249.

[3] J. Praks, A. Kestila, T. Tikka, H. Leppinen, O. Khurshid, M. Hallikainen, AALTO-1 earth observation cubesat mission - Educational outcomes, in: International Geoscience and Remote Sensing Symposium (IGARSS), 2015. doi:10.1109/IGARSS.2015.7326023.

[4] J. Schoolcraft, A. Klesh, T. Werne, MarCO: Interplanetary Mission Development on a CubeSat Scale, in: AIAA SpaceOps Conference, 2016: pp. 1–8. doi:10.2514/6.2016-2491.

[5] A. Klesh, J. Krajewski, MarCO: CubeSats to Mars in 2016, in: 29th Annual AIAA/USU Small Satellite Conference, 2015: pp. 1–7.

[6] L. Mcnutt, L. Johnson, D. Clardy, Near-Earth Asteroid Scout, in: AIAA SPACE 2014 Conference and Exposition, 2014: pp. 1–9. doi:10.2514/6.2014-4435.

[7] A. Marinan, J. Castillo-Rogez, L. Johnson, J. Dervan, C. Seybold, E. Betts, Near Earth Asteroid (NEA) Scout CubeSat Mission, in: 12th Low-Cost Planetary Missions Conference, Pasadena, CA, 2017.

[8] J. Singer, J. Pelfrey, G. Norris, Secondary Payload Opportunities on NASA's Space Launch System (SLS) Enable Science and Deep Space Exploration, in: Space Operations: Contributions from the Global Community, Springer, 2017: pp. 207–220. doi:10.1007/978-3-319-51941-8.

[9] V. Domingo, B. Fleck, A.I. Poland, The SOHO Mission: An Overview, Solar Physics. (1995). doi:10.1007/BF00733425.

[10] T. Prusti, J.H.J. de Bruijne, A.G.A. Brown, A. Vallenari, The Gaia Mission, Astronomy & Astrophysics. (2016). doi:10.1051/0004-6361/201629272.

[11] P. McNamara, G. Racca, Introduction To LISA Pathfinder, 2009.

[12] Space Telescope Science Institute, James Webb Space Telescope Project, Greenbelt, MD, USA, 2004.

[13] ESA, ARIEL - Assessment Study Report, 2017.

[14] ESA, PLATO - Definition Study Report, 2017. http://sci.esa.int/jump.cfm?oid=59252.

[15] K. Lemmer, Propulsion for CubeSats, Acta Astronautica. 134 (2017) 231–243. doi:10.1016/j.actaastro.2017.01.048.

[16] C. Marchal, The Three-body Problem, Elsevier, 1990. https://books.google.co.uk/books?id=AUy2MgEACAAJ.

[17] V. Szebehely, W.H. Jefferys, Theory of Orbits: The Restricted Problem of Three Bodies, Elsevier Ltd, New York, NY, USA, 1967. doi:10.1119/1.1974535.

[18] H. Poincaré, R. Magini, Les Méthodes Nouvelles de la Mécanique Céleste, Il Nuovo Cimento. (1899). doi:10.1007/BF02742713.

[19] CU Aerospace, Propulsion Unit for CubeSats, Champaign, IL, USA, 2017.

[20] Busek, BET-100uN Busek Electrospray Thrust, Natick, MA, USA, 2016.

[21] G. Gómez, A. Jorba, J. Masdemont, C. Simó, Study of the Transfer from the Earth to a Halo Orbit around the Equilibrium Point L1, Celestial Mechanics & Dynamical Astronomy. 56 (1993) 541–562. doi:10.1007/BF00696185.

[22] C. Simó, On the Analytical and Numerical Approximation of Invariant Manifolds, in: Les Méthodes Modernes de La Mecánique Céleste, 1990.

[23] B. Barden, K. Howell, M. Lo, Application of Dynamical Systems Theory to Trajectory Design for a Libration Point Mission, in: Astrodynamics Conference, American Institute of Aeronautics and Astronautics, 1996. doi:doi:10.2514/6.1996-3602.

[24] K. Howell, Three-Dimensional, Periodic, "Halo" Orbits, Celestial Mechanics. 32 (1984) 53. doi:10.1007/BF01358403.

[25] K.C. Howell, H.J. Pernicka, Numerical Determination of Lissajous Trajectories in the Restricted Three-body Problem, Celestial Mechanics. 41 (1987) 107–124. doi:10.1007/BF01238756.

[26] D.L. Richardson, Halo Orbit Formulation for the

ISEE-3 Mission, Journal of Guidance, Control, and Dynamics. 3 (1980) 543–548. doi:10.2514/3.56033.

[27] G. Gómez, J. Llibre, R. Martínez, C. Simó, Dynamics and Mission Design Near Libration Points, World Scientific, 2001. doi:doi:10.1142/4402.

[28] C.L. Goudas, Three-dimensional Periodic Orbits and their Stability, Icarus. 2 (1963) 1–18. https://www.scopus.com/inward/record.uri?eid=2-s2.0-0001790550&partnerID=40&md5=70548d2e5e610cdb15f70449a03d0c20.

[29] C. Markwardt, How to Read the JPL Ephemeris and Perform Barycentering, (2001). https://asd.gsfc.nasa.gov/Craig.Markwardt/bary/ (accessed September 9, 2018).

[30] V.I. Arnold, V. V Kozlov, A.I. Neishtadt, Mathematical Aspects of Classical and Celestial Mechanics (2Nd Ed.), Springer-Verlag, Berlin, Heidelberg, 1997.

[31] Y. Gao, Near-Earth Asteroid Flyby Trajectories from the Sun-Earth L2 for Chang'e-2's Extended Flight, Acta Mechanica Sinica. 29 (2013) 123–131. doi:10.1007/s10409-013-0011-8.

[32] NASA, JPL Center for Near Earth Object Studies, (2008). https://cneos.jpl.nasa.gov/ (accessed January 1, 2018).

[33] NASA, JPL HORIZONS, (2013). http://ssd.jpl.nasa.gov/?horizons (accessed January 1, 2018).

[34] CU Aerospace, Propulsion Unit for CubeSats, Champaign, IL, USA, 2014.

[35] C. Schiff, Adapting Covariance Propagation to Account for the Presence of Modeled and Unmodeled Maneuvers, in: AIAA/AAS Astrodynamics Specialist Conference and Exhibit, American Institute of Aeronautics and Astronautics, 2006. doi:doi:10.2514/6.2006-6294.

[36] A. V. Rao, D. a. Benson, C. Darby, M. a. Patterson, C. Francolin, I. Sanders, G.T. Huntington, GPOPS− II: A MATLAB Software for Solving Multiple-Phase Optimal Control Problems Using hp–Adaptive Gaussian Quadrature Collocation Methods and Sparse Nonlinear Programming, ACM Transactions on Mathematical Software. 37 (2010) 1–39. doi:10.1145/1731022.1731032.

[37] Blue Canyon Technologies, Attitude Determination & Control Systems, Boulder, CO, USA, 2017.

[38] P.S. Jørgensen, J.L. Jørgensen, T. Denver, P. van den Braembuche, The Micro Advanced Stellar Compass for ESA's PROBA 2 Mission, Proceedings of the 5th International Symposium of the IAA on Small Satellites for Earth Observation. (2005) 299–303.

[39] A. Caspi, State of the Art: MinXSS CubeSat Performance and CubIXSS Future Needs, in: Keck Institute for Space Studies Optical Communication on SmallSats Optical Communication on SmallSats, Pasadena, CA, USA, 2017.

[40] Hyperion Technologies B.V., Hyperion Technologies SS200 Sun Sensor, Delft, Netherlands, 2017.

[41] J.P. Mason, M. Baumgart, B. Rogler, C. Downs, M. Williams, T.N. Woods, S. Palo, P.C. Chamberlin, S. Solomon, A. Jones, X. Li, R. Kohnert, A. Caspi, MinXSS-1 CubeSat On-Orbit Pointing and Power Performance: The First Flight of the Blue Canyon Technologies XACT 3-axis Attitude Determination and Control System, Journal of Small Satellites. (2017). http://arxiv.org/abs/1706.06967.

[42] E. Bowell, B. Hapke, K. Lumme, A.W. Harris, D. Domingue, J. Peltoniemi, Application of Photometric Models to Asteroids, Asteroids II. (1988) 524–556. http://adsabs.harvard.edu/abs/1989aste.conf..524B.

[43] C.-I. Lagerkvist, P. Magnusson, Analysis of Asteroid Lightcurves. II. Phase Curves in a Generalized HG-System, Astronomy and Astrophysics Supplement Series. 86 (1990) 119–165.

[44] W.E. Wiesel, Modern Orbit Determination, 2nd ed., Aphelion Press, Beavercreek, OH, USA, 2003.

[45] N.E. Bowles, C. Snodgrass, A. Gibbings, J.P. Sanchez, J.A. Arnold, P. Eccleston, T. Andert, A. Probst, G. Naletto, A.C. Vandaele, J. de Leon, A. Nathues, I.R. Thomas, N. Thomas, L. Jorda, V. Da Deppo, H. Haack, S.F. Green, B. Carry, K.L. Donaldson Hanna, J. Leif Jorgensen, A. Kereszturi, F.E. DeMeo, M.R. Patel, J.K. Davies, F. Clarke, K. Kinch, A. Guilbert-Lepoutre, J. Agarwal, A.S. Rivkin, P. Pravec, S. Fornasier, M. Granvik, R.H. Jones, N. Murdoch, K.H. Joy, E. Pascale, M. Tecza, J.M. Barnes, J. Licandro, B.T. Greenhagen, S.B. Calcutt, C.M. Marriner, T. Warren, I. Tosh, CASTAway: An Asteroid Main Belt Tour and Survey, Advances in Space Research. (2017). doi:10.1016/j.asr.2017.10.021.

[46] B. Segret, D. Hestroffer, G. Quinsac, M. Agnan, J. Vannitsen, B. Mosser, In-flight orbit determination for a deep space CubeSat, in: 2018 IEEE Aerospace Conference, Institute of Electrical and Electronics Engineers Inc., 2018: pp. 1–12. doi:10.1109/AERO.2018.8396756.

2018-10-05

# Low-energy trajectory design and autonomous navigation to flyby near-Earth asteroids using CubeSats

Machuca, Pablo

International Astronautical Federation

Pablo Machuca, Joan Pau Sánchez, Josep J. Masdemont and Gerard Gómez. Low-energy trajectory design and autonomous navigation to flyby near-Earth asteroids using CubeSats. 69th þÿInternational Astronautical Congress, 2018 (IAC 18), 1-5 October 2018, https://iafastro.directory/iac/archive/